Reynolds-averaged Navier-Stokes simulations of the flow past a leading edge inflatable wing for airborne wind energy applications

Viré, Axelle; Demkowicz, Patryk; Folkersma, Mikko; Roullier, Arthur; Schmehl, Roland

DOI
10.1088/1742-6596/1618/3/032007

Publication date
2020

Document Version
Final published version

Published in
Journal of Physics: Conference Series

Citation (APA)
Viré, A., Demkowicz, P., Folkersma, M., Roullier, A., & Schmehl, R. (2020). Reynolds-averaged Navier-Stokes simulations of the flow past a leading edge inflatable wing for airborne wind energy applications. *Journal of Physics: Conference Series*, *1618*(3), Article 032007. https://doi.org/10.1088/1742-6596/1618/3/032007

Journal of Physics: Conference Series

Reynolds-averaged Navier-Stokes simulations of the flow past a leading edge inflatable wing for airborne wind energy applications

To cite this article: Axelle Viré *et al* 2020 *J. Phys.: Conf. Ser.* **1618** 032007

The Science of Making Torque from Wind (TORQUE 2020) IOP Publishing
Journal of Physics: Conference Series **1618** (2020) 032007 doi:10.1088/1742-6596/1618/3/032007

Reynolds-averaged Navier-Stokes simulations of the flow past a leading edge inflatable wing for airborne wind energy applications

Axelle Viré, Patryk Demkowicz, Mikko Folkersma, Arthur Roullier, and Roland Schmehl

Faculty of Aerospace Engineering, Delft University of Technology, Kluyverweg 1, 2629 HS Delft, The Netherlands

E-mail: `a.c.vire@tudelft.nl`

Abstract. In this work we present Reynolds-averaged Navier-Stokes (RANS) simulations of the flow past the constant design shape of a leading-edge inflatable (LEI) wing. The simulations are performed with a steady-state solver using a $k-\omega$ SST turbulence model, covering a range of Reynolds numbers between $10^5 \leq$ and $\leq 15 \times 10^6$ and angles of attack varying between -5° and 24°, which are representative for operating conditions in airborne wind energy applications. The resulting force distributions are used to characterize the aerodynamic performance of the wing. We found that a $\gamma - \bar{\mathrm{Re}}_\theta$ transition model is required to accurately predict the occurrence of stall up to at least Re= 3×10^6. The work highlights similarities with the flow past a two-dimensional LEI airfoil, in particular, with respect to flow transition and its influence on the aerodynamic properties. The computed values of the lift and drag coefficients agree well with in-flight measurements acquired during the traction phase of the LEI wing operation. The simulations show that the three-dimensional flow field exhibits a significant cross flow along the span of the wing.

1. Introduction

In recent years, the size and height of conventional horizontal wind turbines have not ceased to increase in view of harnessing ever larger quantities of wind energy. This increase however brings structural challenges to the design of future wind turbines. One of the promising alternatives to harness wind energy at increasing altitudes is to use a flying device that is tethered to the ground. There are different concepts and modes of operation of such airborne wind energy (AWE) devices [3, 26]. A prominent example is to fly a wing crosswind and tether it to a generator on the ground. The aerodynamic force on the wing reels out the tether and turns a drum, hence generating mechanical power that can be converted to electrical power. Although these AWE devices present several advantages compared to conventional wind turbines, they face also many challenges for large-scale commercial deployment. One of them is related to the lack of knowledge and reference data concerning the aerodynamics of such wings. The understanding of the flow dynamics past the wing is however important to improve the system design and, to some extent, relate to the structural deformations observed during flight.

The present work focusses on the aerodynamics of a LEI wing, which consists of an inflated tubular frame with an attached membrane canopy. The aerodynamic load on the canopy is transferred to the tubular frame and from there via multiple bridle lines to the tether. As a consequence of the lightweight flexible construction, the entire wing deforms during flight. This aeroelastic behavior significantly influences the flow field and the aerodynamic performance of LEI wings. For the purpose of simplicity, the strut tubes are omitted in this paper and the wing is assumed to be rigid so that fluid-structure interactions are neglected. The present study has two primary objectives, firstly, to better understand the fundamental flow phenomena governing the aerodynamics of LEI wings and, secondly, to provide reference data to verify aerodynamic simulation tools for thin membrane wings.

The aerodynamics of LEI wings, also called sailwings, has been investigated to some extent experimentally and numerically in the literature. Potential flow methods with viscous corrections have been used, both in the context of airborne wind energy and sailing. For example, Fiddes and Gaydon [9] used a 3D free wake vortex lattice method (VLM) combined with an integral boundary layer method to correct for viscous effects on yacht sails. Lorillu et al. [17] developed a potential flow method with a Helmholtz thick wake model to aid prediction of flow separation on 2D yacht sails. The resultant sail shape and free streamline computed with this approach were in good agreement with experimental data, for both attached and separated flows. Graf et al [12] used a lifting line method combined with lift and drag airfoil data obtained through 2D RANS simulations for analysis of wing sails. Similarly, Vimalakanthan et al [29] used a non-linear lifting line model and a free vortex code combined with polar data obtained from 2D CFD for the power prediction analysis of an energy harvesting airplane. Potential flow methods have also been applied to flows around LEI wings. Gaunaa et al. [11] present an efficient method for determining aerodynamic performance of such a wing by using VLM coupled with 2D airfoil data to take into account effects of airfoil thickness and fluid viscosity. The method achieved good agreement with a 3D RANS simulation of a simplified kite geometry, especially for attached flow. Similarly to other studies including potential flow methods, the correlation worsens as the flow undergoes severe separation. Leuthold [16] investigated the aerodynamics of a 3D LEI wing using a quasi-steady multiple wake vortex lattice method and compared the results to experimental measurements, 3D lifting line model and 3D RANS simulations. It was found that the model struggles to predict pressure side flow reattachment correctly, which is very common to occur on LEI wings during flight.

In light of the limitations of potential flow methods, computational fluid dynamics (CFD) models that solve the Navier–Stokes equations have also been used. For example, Kheiri et al [14] applied modified actuator disc theory to a crosswind kite power system and compared power production results with URANS and a $k-\epsilon$ turbulence model. The study assumed fully turbulent attached flow in all cases and considered a straight rigid wing. When applied to separated flows, the $k-\epsilon$ model fails to accurately predict lift and drag coefficients, even if the prediction is better than when using potential flow methods [4]. Smith and Shyy [27] performed an analysis of viscous turbulent flow over 2D flexible membranes using the $k-\omega$ SST turbulence model and found better results than with a $k-\epsilon$ model when investigating single-surface membrane wing aerodynamics. The $k-\omega$ SST has also been applied to both 2D aeroelastic applications [28], yacht sails [30] and LEI wing analyses [6, 7, 25]. Popular turbulence models, such as the $k-\omega$ SST model, assume that the boundary layer is always turbulent, as they cannot model the transition from laminar to turbulent flow. Folkersma et al [10] investigated boundary layer transition of a LEI airfoil using the $k-\omega$ SST turbulence model with a $\gamma-\bar{\mathrm{R}}\mathrm{e}_\theta$ transition model. Their results were in agreement with experimental data at relatively low Reynolds numbers ($\mathrm{Re}=10^5$) over all the considered angles of attack. The results obtained from simulations with the transition model were closer to the experimental values than the ones obtained without transition model. The $k-\omega$ SST turbulence model with $\gamma-\bar{\mathrm{R}}\mathrm{e}_\theta$ transition was also used to validate a new potential flow method using vortex elements [11].

Besides numerical studies, experimental analyses have been described in the literature.

However, wind tunnel experiments for airborne wind energy devices can be very challenging, especially in the context of LEI wings, because the thin membrane canopy cannot be scaled down easily. Experimental studies on single membrane sailwing sections are available at moderate Reynolds numbers [2, 1]. Field tests have also been performed more recently for airborne wind energy wings. One option are tow tests, for which the wing is tethered to a moving vehicle, to measure both static flight performance and dynamic flight history [5, 23, 13, 24]. This testing method is however limited in terms of maximum traction force. There are also measurement uncertainties due to wind variations and limitations in the measurement of lift-to-drag ratios for dynamic maneuvers [22]. Alternatively, the flow past the wing can be measured in situ using on-board sensors [21].

Despite these studies, there is still a lack of reference data for the detailed aerodynamics of LEI wings. The objective of this work is to provide numerical data for the aerodynamics of a LEI wing, in order to better understand the flow phenomena and to support future model validation in the context of airborne wind energy. It will also assess the importance of 3D flow effects on aerodynamic performances, by comparing with the work of Folkersma et al [10] which was performed in 2D with the same airfoil section. The paper is organised as follows. Section 2 presents the numerical approach used to solve the flow problem, including numerical methods, meshes and turbulence modelling. Section 3 presents the results for different Reynolds numbers and angles of attack, as well as comparison with in-flight measurement data. Flow visualisations are also provided. Finally, Section 4 summarises the main observations of the study.

2. Methodology

2.1. Fluid dynamics equations

The open-source CFD solver Open-FOAM-v1812 is used in this study. The solver is based on a finite-volume discretisation of the incompressible steady-state Reynolds-averaged Navier–Stokes equations for a Newtonian fluid, see for example [31]. These equations are closed by a $k-\omega$ SST turbulence model [20]. The specific implementation of the model is that presented by [19], with a revised turbulence specific dissipation rate production term from [18]. The detailed equations are available in the literature, see for example [10]. As it will be shown in Section 3, the use of a transition model is needed to get accurate results over a large range of Reynolds numbers. Here, the $\gamma - \widetilde{\mathrm{Re}}_{\theta t}$ model [15] is adopted. This is a correlation-based model that uses empirical transition correlations obtained from experimental databases covering a variety of geometries and flow conditions. As such, it does not attempt to capture the actual physics of the flow transition. The model uses an intermittency parameter γ, that represents the probability for a point in the flow field to be located in the turbulent region. The transport equation for the intermittency is based on the wall distance and the local flow field quantities. It is given by

$$\frac{\partial \gamma}{\partial t} + \frac{\partial \gamma u_j}{\partial x_j} = P_\gamma - D_\gamma + \frac{\partial}{\partial x_j}\left[\left(\nu + \frac{\nu_t}{\sigma_f}\right)\frac{\partial \gamma}{\partial x_j}\right], \tag{1}$$

in which

$$P_\gamma = F_{\mathrm{length}} c_{a1} \left|\frac{\partial u}{\partial y}\right| \left(\gamma F_{\mathrm{onset}}\right)^{1/2} \left(1 - c_{e1}\gamma\right), \tag{2}$$

where the function F_{length} controls the transition length and its correlation is given in [15], and y is the distance from the nearest wall. Furthermore, F_{onset} controls the transition onset and quickly grows from 0 to 1 when the boundary layer becomes turbulent, based on the ratio between the vorticity Reynolds number $\mathrm{Re}_\nu = \frac{y^2}{\nu}\left|\frac{\partial u}{\partial y}\right|$ and the critical momentum thickness Reynolds number $\mathrm{Re}_{\theta c}$. The expression for the latter is also given by a correlation, as detailed in [15]. Both correlations for $\mathrm{Re}_{\theta c}$ and F_{length} are a function of the local transition onset momentum thickness Reynolds number $\widetilde{\mathrm{Re}}_{\theta t}$. The function F_{onset} activates an intermittency source term and leads to turbulence production. The destruction term, or relaminarisation source, is defined as

$$D_\gamma = c_{a2}\Omega\gamma F_{\text{turb}}\left(c_{e2}\gamma - 1\right), \tag{3}$$

where Ω stands for the vorticity magnitude. The function F_{turb} is designed to disable intermittency destruction outside of the laminar boundary layer or in the viscous sublayer and is given by

$$F_{\text{turb}} = e^{\left(-\frac{\mathrm{R}_T}{4}\right)^4}, \tag{4}$$

with $\mathrm{R}_T = k/(\nu\omega)$. Finally, the intermittency is modified to be able to exceed $\gamma = 1$ during the laminar boundary layer separation, in order to improve the prediction of separation-induced transition. Thus,

$$\gamma_{\text{sep}} = \min\left(s_1 \max\left[0, \left(\frac{\mathrm{Re}_\nu}{3.235 Re_{\theta c}}\right) - 1\right] F_{\text{reattach}}, 2\right) F_{\theta t}, \tag{5}$$

where $F_{\text{reattach}} = e^{-\left(\frac{\mathrm{R}_T}{20}\right)^4}$ and $s_1 = 2$. A second transport equation is formulated for the local transition onset momentum thickness Reynolds number $\widetilde{\mathrm{Re}}_{\theta t}$ and is expressed as

$$\frac{\partial \widetilde{\mathrm{Re}}_{\theta t}}{\partial t} + \frac{\partial \widetilde{\mathrm{Re}}_{\theta t} u_j}{\partial x_j} = P_{\theta \mathrm{t}} + \frac{\partial}{\partial x_j}\left[\sigma_{\theta t}\left(\nu + \nu_t\right)\frac{\partial \widetilde{\mathrm{Re}}_{\theta t}}{\partial x_j}\right]. \tag{6}$$

In the free stream, the source term $P_{\theta t}$ forces $\widetilde{\mathrm{Re}}_{\theta t}$ to match the local value of $\mathrm{Re}_{\theta t}$ that is determined from the empirical correlations,

$$P_{\theta t} = \frac{c_{\theta t}}{t}\left(\mathrm{Re}_{\theta t} - \widetilde{\mathrm{Re}}_{\theta t}\right)\left(1 - F_{\theta t}\right), \tag{7}$$

where $t = \frac{500\nu}{U^2}$ is a time scale and U represents the velocity magnitude. The function $F_{\theta t}$ turns off the source term within the boundary layer, thus enabling diffusion of $\widetilde{\mathrm{Re}}_{\theta t}$ from the free stream into the boundary layer. It is expressed as

$$F_{\theta t} = \min\left(\max\left(F_{\text{wake}} \cdot e^{-\left(\frac{y}{\delta}\right)^4}, 1 - \left(\frac{\gamma - 1/c_{e2}}{1 - 1/c_{e2}}\right)^2\right), 1\right), \tag{8}$$

with

$$\delta = \frac{375\Omega y}{U^2}\widetilde{\mathrm{Re}}_{\theta t}\nu, \quad F_{\text{wake}} = e^{-\left(\frac{\mathrm{Re}_\omega}{10^5}\right)^2}, \quad \mathrm{Re}_\omega = \frac{\omega y^2}{\nu}. \tag{9}$$

Furthermore, the function F_{wake} turns off $F_{\theta t}$ in the wake regions. The values of the model constants are: $c_{e1} = 1$, $c_{a1} = 2$, $c_{e2} = 50$, $c_{a2} = 0.06$, $\sigma_f = 1$, $c_{\theta t} = 0.03$, and $\sigma_{\theta t} = 2$.The transition model is integrated in the $k-\omega$ SST turbulence model by scaling the production term of the original transport equation for k with γ_{eff} and the destruction term as

$$\widetilde{D}_k = \min\left(\max\left(\gamma_{\text{eff}}, 0.1\right), 1.0\right) D_k, \tag{10}$$

where $\gamma_{\text{eff}} = \max\left(\gamma, \gamma_{\text{sep}}\right)$. The transition model also modifies the blending function F_1 of the original $k-\omega$ SST turbulence model, in order to prevent switching to the $k-\epsilon$ model within a laminar boundary layer, i.e.

$$F_1 = \max\left(F_1, F_3\right), \quad F_3 = e^{-\left(\frac{R_y}{120}\right)^8}, \quad R_y = \frac{y\sqrt{k}}{\nu}. \tag{11}$$

In terms of discretisation, the continuity and momentum equations are discretised using second-order methods. The equations for k, ω and the transition model are solved using a first-order upwind scheme. All simulations were run for 4000 iterations, although convergence was reached after 1000 iterations in most cases, with normalised residuals between 10^{-5} and 10^{-6}. Only when the wing is in stall, the largest residuals were between 10^{-4} and 10^{-5}.

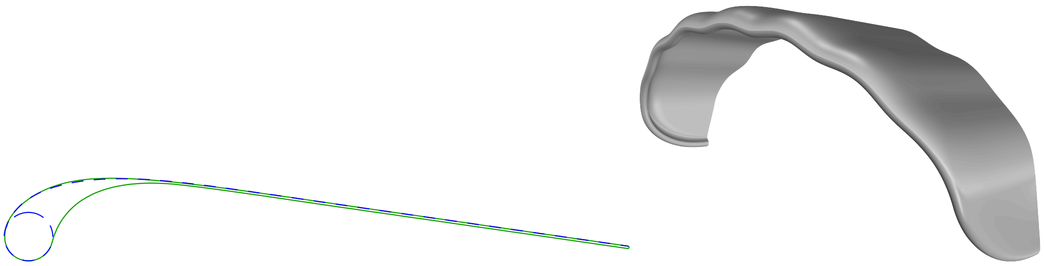

Figure 1. Left: Original (dashed line) and filled in (solid line) profile at the wing symmetry plane. Right: LEI V3A CAD model. Figures taken from [8].

2.2. Meshing

The wing geometry considered here is the LEI V3A wing, as described in [8]. It is the nominal design shape without any deformations. Generating a high quality volume mesh for this wing is non-trivial due to the inflated leading edge, the very thin canopy, and the large anhedral angle. The original geometry was exported from the kite design software Surfplan$^{\mathrm{TM}}$ to a format readable by the Computer Aided Design software Rhinoceros. Multiple simplifications and enhancements were made. First, the bridle system and chordwise struts were removed. Second, the membrane canopy was given a small thickness with a rounded trailing edge to fulfill the requirements of the meshing software. A small filling behind the leading edge was added to improve the mesh quality in that region. As shown by [7], such a filling has a negligible effect on the flow solution. The filling originates from the leading edge tube at about 60° angle and connects to the lower surface of the canopy at about 25% of the chord length. Both the original and the modified profiles are shown in Fig. 1 (left), whilst Fig. 1 (right) shows the resulting 3D CAD model. The wing is placed in a circular domain whose radius equals to $100c$, c being the wing chord in the symmetry plane. A hybrid structured and unstructured mesh was generated using the T-Rex algorithm of mesh-generation software Pointwise$^{®}$. This uses a structured mesh in the boundary layer and near-wall region, and an unstructured mesh in the far field. The detailed meshing procedure is described in [8]. The surface mesh of the wing and the volume mesh of the computational domain are shown in Fig. 2 (left) and Fig. 2 (right), respectively. A mesh convergence study was performed with six different meshes but keeping the height of the smallest cell close to the wing boundary such that $y^+ < 1$. It was found that a mesh with 330 points along the leading edge in the spanwise direction, 120 points along the airfoil profile, and a cell growth ratio of 1.15 in the boundary layer, leads to sufficiently accurate and converged results. Overall, this gives a mesh containing approximately 6 million cells and this was used for all the results presented in this paper. At the inlet, the magnitude of the velocity field is set to unity and its direction varies depending on the desired angle of attack. The pressure gradient is set to zero. The turbulence intensity is set to 0.02 and the ratio of eddy viscosity to physical viscosity equals 10. Finally, $\gamma = 1$ and $\widetilde{\mathrm{Re}}_{\theta t}$ is calculated using the empirical correlations. At the outlet, the pressure is set to zero and a zero gradient is prescribed for the velocity field and the turbulence quantities. A no-slip boundary condition is applied at the wing surface. At the walls, both γ and $\widetilde{\mathrm{Re}}_{\theta t}$ experience a zero normal flux. The model requires that the first cell near the wall satisfies $y^+ \approx 1$, in order to capture the transitional boundary layer adequately. Finally, a symmetry boundary condition is imposed at the plane of symmetry, so that only half of the wing is modelled.

3. Results

Figure 3 shows the lift and drag polars of the three-dimensional wing for a range of Reynolds numbers $10^5 \leq \mathrm{Re} \leq 15 \times 10^6$ and angles of attack varying between $-5°$ and $24°$. It is worth

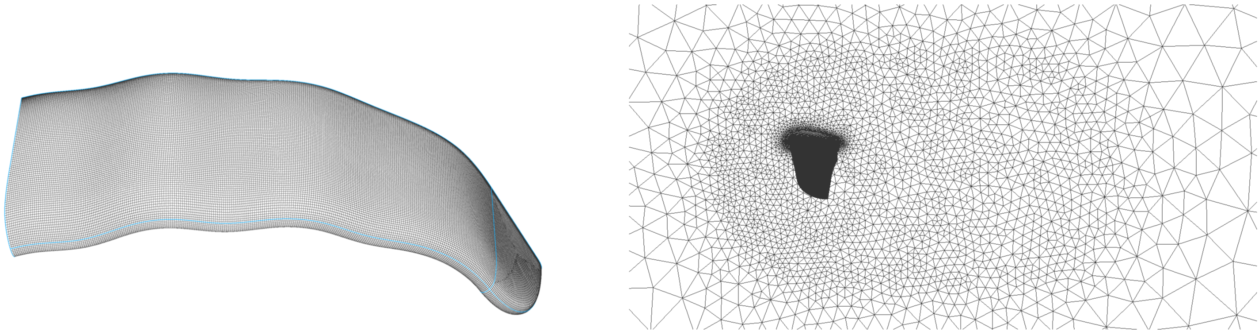

Figure 2. Left: Surface mesh of the wing. Right: Volume mesh of the computational domain. Figures taken from [8].

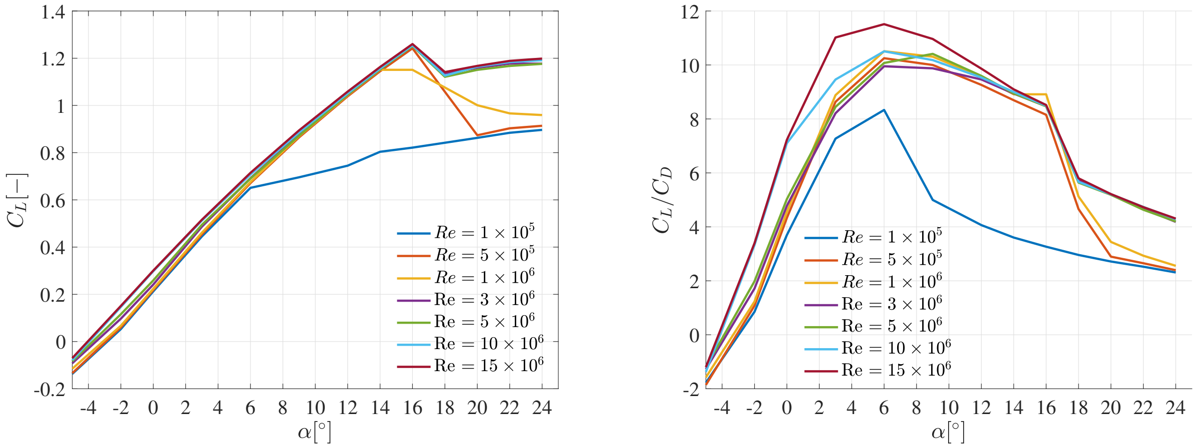

Figure 3. Lift coefficient (left) and ratio of lift-to-drag coefficients (right) for the LEI wing computed at various Reynolds numbers.

noting that, due to the choice of solver that is steady-state, the results for angles of attack before stall are considered most reliable. The results at stall and post-stall are mostly indicative, knowing that the same model did give accurate results in these conditions for the two-dimensional flow past a sailwing [10]. In Fig. 3, it is apparent that the lowest considered Reynolds number of $\mathrm{Re} = 10^5$ gives significantly different results than the others, as flow separation occurs directly from a laminar boundary layer. The angle of attack at which stall occurs increases with Re, until $\mathrm{Re} = 10^6$, at which point it decreases until $\mathrm{Re} = 10^7$. For $\mathrm{Re} > 10^7$, the stall angle and maximum lift coefficient increase again. Interestingly, this behavior was already observed in the two-dimensional simulations of [10]. This behaviour can be explained by the mechanism of flow transition and can therefore only be captured when a transition model is used. Before giving more insight into the mechanism of flow transition, simulation results with and without transition models are compared. Figure 4 shows the lift (left) and drag (right) coefficients at three Reynolds numbers with (solid line) and without (dashed line) transition model. It is shown that the lift and drag coefficients with and without transition model agree well for angles of attack before stall for all the Reynolds numbers considered. At stall, however, discrepancies are obtained for both the lift and drag coefficient for $\mathrm{Re} = 5\times10^5$ and $\mathrm{Re} = 3\times10^6$. As expected, the need for a transition model decreases at higher Reynolds numbers. Similar observations are made when analysing the skin friction coefficient at the surface of the wing. Here, the chordwise

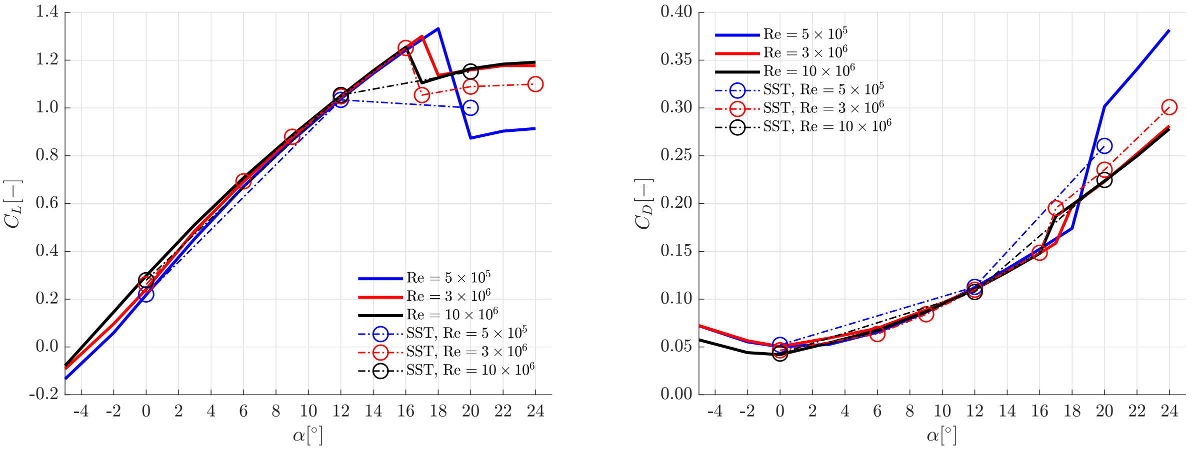

Figure 4. Lift (left) and drag (right) polars for the LEI wing computed at various Reynolds numbers, with (solid line) and without (dashed line) transition model. Figures taken from [8].

skin friction coefficient is calculated as

$$c_f = \frac{2\tau_{w,x}}{\rho U_\infty^2}, \tag{12}$$

where $\tau_{w,x}$ is the wall shear stress in the chordwise direction defined as

$$\tau_{w,x} = \mu \frac{\partial U_x}{\partial y}\bigg|_{y=0}. \tag{13}$$

Negative values of c_f indicate regions of flow recirculation, while a sudden increase in skin friction represents laminar to turbulent transition. Figure 5 shows the skin friction coefficient at the suction side of the wing, for three Reynolds numbers (increasing from left to right) and an angle of attack of $\alpha = 12°$. Results are shown with (top) and without (bottom) transition model. At the lowest Reynolds number, the surface plots with transition model show a distinct laminar separation bubble across the whole span of the wing. This bubble vanishes at $\mathrm{Re} = 3 \times 10^6$, where the boundary layer transitions before flow separation. These flow phenomena are absent when the $k - \omega$ SST model is used without transition model. For $\mathrm{Re} = 10^7$, the boundary layer transitions very early on the suction side of the wing. Thus, the results with and without transition model are similar. To give more insight into this, Fig. 6 shows the chord-wise pressure and skin friction coefficients at the symmetry plane for $\alpha = 6°$ and various Reynolds numbers. Only results with transition model are presented. Note that the reference chord c_{ref} is the distance between the attachment point of the bridle system and the trailing edge, as presented in [21]. It can be observed that the laminar separation bubble present for $10^5 < \mathrm{Re} < 10^6$ begins at approximately the same point for all the Reynolds numbers, namely $x/c_{ref} = 0.16$, and its size diminishes with increasing Re. At $\mathrm{Re} = 10^6$, the laminar separation bubble almost vanishes and the laminar boundary layer is the longest. These characteristics lead to a large lift coefficient and a low drag coefficient, compared to those at other Reynolds numbers. As the Reynolds number increases to $\mathrm{Re} = 10^7$, the transition point moves towards the leading edge and the height of the separation bubble decreases. The height of the separation bubble effectively changes the apparent camber of the wing. Thus. the smaller the height of the separation bubble, the smaller the lift coefficient. For $\mathrm{Re} > 10^7$, the boundary layer is fully turbulent which leads to a new increase in the maximum lift coefficient and stall angle.

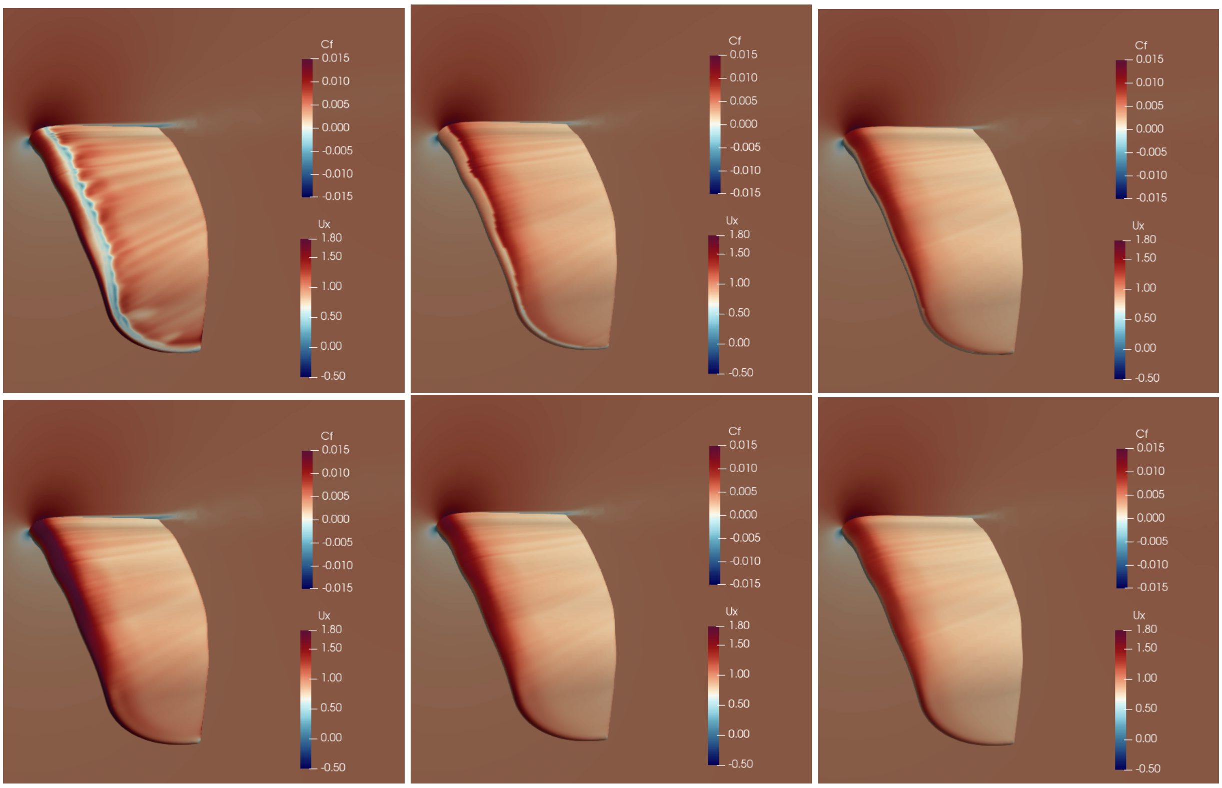

Figure 5. Skin friction coefficient at the suction side of the wing for an angle of attack of $\alpha = 12°$ and three Reynolds numbers: $\mathrm{Re} = 5 \times 10^5$ (left), $\mathrm{Re} = 3 \times 10^6$ (centre), and $\mathrm{Re} = 10^7$ (right). Results are shown with (top) and without (bottom) transition model. Figures taken from [8].

Another feature of the C_L/C_D plots is a noticeable difference between the results for $\mathrm{Re} \geq 10^7$, especially at small angles of attack. As explained in [10], this difference can be attributed to the drag crisis occurring at the cylindrical leading-edge tube. Based on the dimensions of the leading edge, the drag crisis for the leading edge of the present wing is expected at a chord-based Reynolds number of about $\mathrm{Re} = 10^7$. This corresponds to a critical flow, for which a cylinder experiences significantly reduced drag and a smaller recirculation zone downstream. It is caused by the laminar to turbulent flow transition occurring before the typical laminar separation point, resulting in the separation point moving significantly further downstream. This is also observed in the present results, for which the recirculation zone at $\mathrm{Re} = 10^7$ is much smaller than that at lower Reynolds numbers (not shown here). For smaller Reynolds numbers, the flow separates from the laminar boundary layer on the pressure side of the LE tube, hence increasing the drag coefficient and the recirculation zone on the pressure side.

Figure 7 further compares the numerical results with some experimental data obtained during operation of the kite power system [21]. The wing is identical to that considered in the CFD simulations, except for the presence of struts. During flight, the wing follows a figure-of-eight path. However, the experimental data is plotted for the straight flight segments on the flight path during crosswind operation. The turns and the retraction phases are filtered out for the sake of comparison with the numerical results. On the straight flight segments, a small amount of steering is still required to create a side force which balances the effect of gravity. The experimental data was generated from a flight test conducted on 8 October 2019. Note that the V3 wing used here is from an early design of the kite power system, and therefore, the data

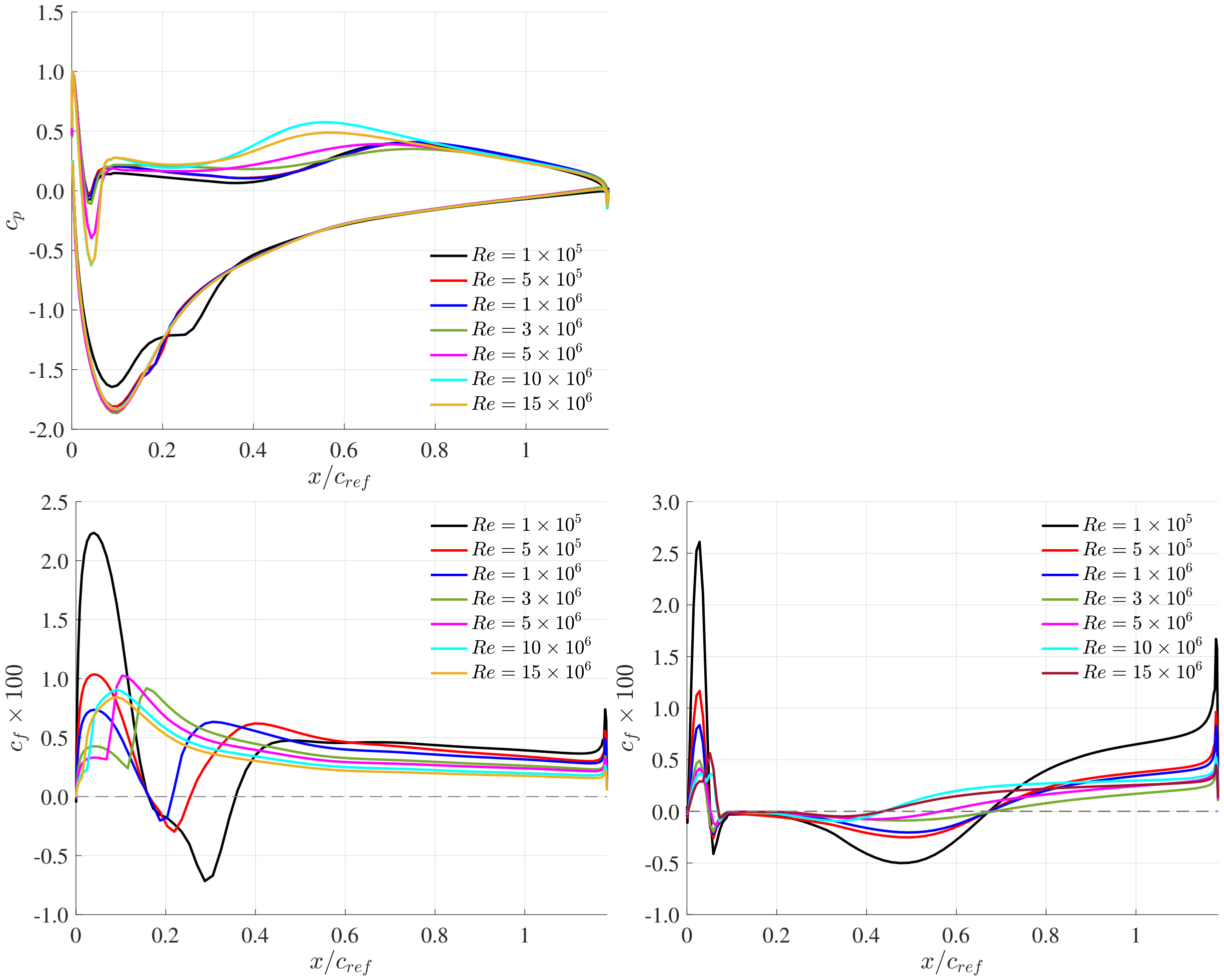

Figure 6. Pressure coefficient (top) and skin friction coefficient (bottom) along kite surface at the symmetry plane for $\alpha = 6°$ and different Re: suction side (left) and pressure side (right). The reference chord length is denoted by c_{ref}.

does not reflect the state-of-art in airborne wind energy production. The statistics were analysed using the model-based system identification algorithm described in [21] on a more extensive data set covering 128 complete pumping cycles, each containing 6 figure-of-eight maneuvers. For the experimental conditions to be as close as possible to the conditions used for the CFD analysis, only the upwards-directed straight flight segments of the acquired data were taken into account, resulting in 768 individual data points. The apparent wind speed used for the estimation of the aerodynamic coefficients was directly measured with a Pitot tube suspended in the bridle line system of the wing. The average measured apparent wind speed for all accounted data points is 18.96 m/s, and the corresponding average Reynolds number is 3.9×10^6. Figure 7 (left) shows the lift coefficient as a function of angle of attack. Experimentally, the calculation of these quantities is detailed in [21]. The angle of attack is measured with respect to the heading vector of the kite. The forces are measured with respect to the tether angles and corrected to account for the difference in angle. Although there are clear discrepancies between numerical and experimental data, such a comparison has never been shown before and can provide indicative results. One of the difference between numerical and in-flight data stems from the fact that the wing deforms during flight, which lowers its aerodynamic performance, and is not taken into account in the

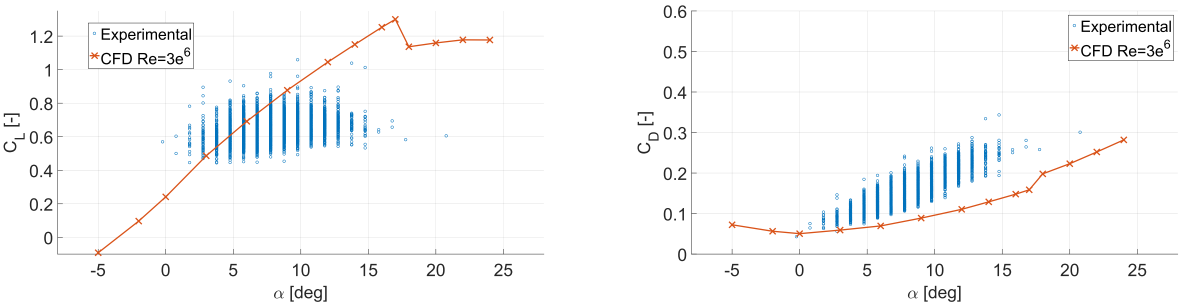

Figure 7. Comparison between CFD and in-flight measurements for the lift (left) and drag (right) coefficients as a function of angle of attack.

numerical simulations. Also, the kite slightly rolls in flight, which shifts part of the lift into a side force component. Figure 7 (right) shows that the measured drag coefficients are larger than the computed ones. As for the lift coefficient, the wing deformation affects its aerodynamic performance, hence increasing drag. In fact, flight tests on this wing have shown that the wing does not only deform in the spanwise direction (the tips being pulled in) but that there is also a distinct kink in the chord at around 15% from the leading edge at high force. Both these deformations result in a higher drag force and explain the discrepancies with the CFD data. Note that these effects have been solved in the newer designs of the kite power system. Another effect that also explains the difference between CFD and experimental drag forces is due to the orientation of the tether at the attachment point. In particular, an increase in the angle between the tether and the kite diminishes the values of the drag coefficient by 0.015 on average, whilst only the spread of the lift coefficient is affected. Thus, the wing orientation partly explains the difference in drag coefficient. Another effect comes from the asymmetry caused by the steering of the wing, which increases the drag coefficient by a value of 0.01 on average. Therefore, wing deformation, orientation of the tether and steering of the wing are believed to be the main factors explaining the discrepancies between measurements and CFD data. Note that the drag associated with the bridle line is believed to have a negligible effect on the overall lift and drag coefficients.

Lastly, flow visualisations are provided in Fig. 8 for $\mathrm{Re} = 3 \times 10^6$ and an angle of attack $\alpha = 12^\circ$. The left figure shows the streamlines colored by the magnitude of the component of the velocity normal to the symmetry plane. On the suction side, the flow tends to move inwards, whilst it moves outwards on the pressure side. Also, there is a non-uniform flow recirculation zone behind the leading edge. This was observed for all the angles of attack considered and is illustrated in Fig. 8 (right) through the contours of the streamwise component of the flow velocity along the wing span, at a streamwise location $x = 0.3$.

4. Conclusions

This work provides numerical data for the aerodynamic performance of a leading-edge inflatable wing under a range of flow conditions that are representative for the operation of airborne wind energy systems. The simulations were performed using a steady-state RANS solver with a $k - \omega$ SST turbulence model and a flow transition model. It is shown that the transition model was required to accurately predict the occurrence of stall up to at least $\mathrm{Re} = 3 \times 10^6$. It is important to note, however, that the present results at stall and post-stall conditions should be considered with care due to the use of a steady-state solver. Further work is needed at these conditions using unsteady and higher-fidelity models in order to confirm the present results. Despite the limitations of the solver, the polars show similar trends to the results of a two-dimensional

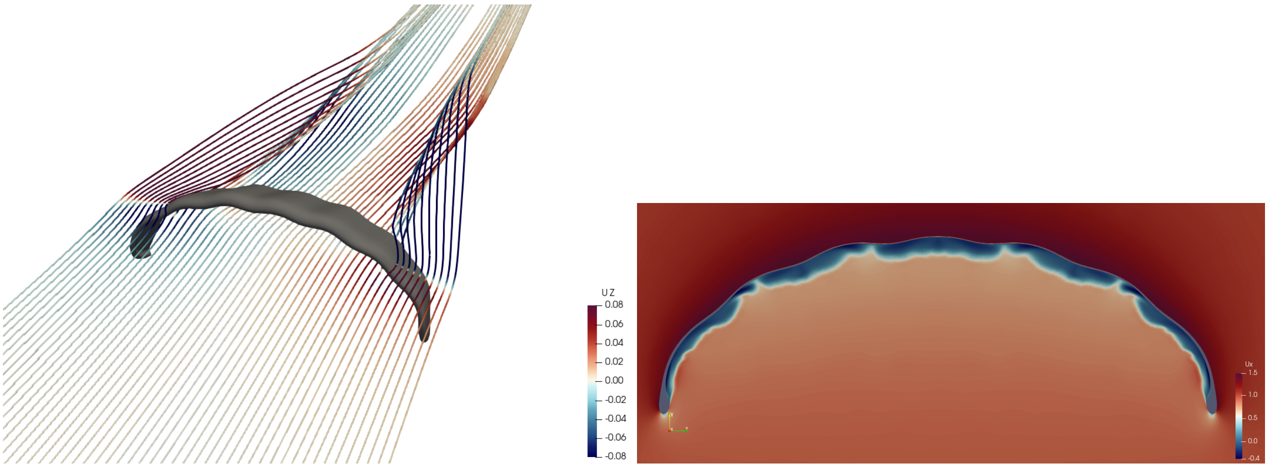

Figure 8. Visualisations for Re = 3×10^6 and $\alpha = 12°$. Left: Streamlines colored by the magnitude of the component of the velocity normal to the symmetry plane U_z. Right: Contours of the streamwise component of the flow velocity along the wing span, at $x = 0.3$. Figures taken from [8].

flow past a LEI airfoil. The results also highlight a large amount of cross flow along the span of the wing. Finally, additional insights are provided based on a comparison with in-flight measurements. In future work, the influence of the presence of struts on the wing will also need to be further investigated.

Acknowledgments

Axelle Viré acknowledges support from the European Commission under the H2020 project TWIND (grant agreement no. 857631) and the Rijksdienst voor Ondernemend Nederland (RVO) through the TSE Hernieuwbare Energie funding scheme (ABIBA and TouchWind projects). Mikko Folkersma and Roland Schmehl acknowledge support from the European Commission under the H2020-ITN project AWESCO (Marie Skłodowska-Curie grant agreement No. 642682). The authors would like to thank Kitepower B.V. (`http://kitepower.nl/`) for providing the flight data that allowed them to determine measured aerodynamic coefficients.

References

[1] R. Boer. Low speed aerodynamic characteristics of a two-dimensional sailwing with adjustable slack of the sail. Technical Report Report LR-307, Delft University of Technology, 1980.
[2] A. Bruining. Aerodynamic characteristics of a curved plate airfoil section at Reynolds numbers 60.000 and 100.000 and angles of attack from -10 to +90 degrees. Technical Report Report LR-281, Delft University of Technology, 1979.
[3] A. Cherubini, A. Papini, R. Vertechy, and M. Fontana. Airborne wind energy systems: A review of the technologies. *Renewable and Sustainable Energy Reviews*, 51:1461–1476, 2015.
[4] S. Collie, M. Gerritsen, and M. O'Sullivan. Numerical simulation of the turbulent flow past upwind yacht sails. *ournal of Wind Engineering and Industrial Aerodynamics*, 91(2), 2002.
[5] G.M. Dadd, D.A. Hudson, and R.A. Shenoi. Comparison of two kite force models with experiment. *Journal of Aircraft*, 47(1):212–224, 2010.
[6] A. de Wachter. Deformation and aerodynamic performance of a ram-air wing. Master's thesis, Delft University of Technology, 2008.
[7] M. Deaves. An investigation of the non-linear 3D flow effects relevant for leading edge inflatable kites. Master's thesis, Delft University of Technology, 2015.
[8] P. Demkowicz. Numerical analysis of the flow past a leading edge inflatable kite wing using a correlation-based transition model. Master's thesis, Delft University of Technology, 2019.

[9] S.P. Fiddes and J.H. Gaydon. A new vortex lattice method for calculating the ow past yacht sails. *Journal of Wind Engineering and Industrial Aerodynamics*, 63(1):35–59, 1996.
[10] M. Folkersma, R. Schmehl, and A. Viré. Boundary layer transition modeling on leading edge inflatable kite airfoils. *Wind Energy*, pages 1–14, 2019.
[11] M. Gaunaa, P.F. Paralta Carqueija, P.M. Réthoré, and N.N. Sorensen. A computationally efficient method for determining the aerodynamic performance of kites for wind energy applications. In *European Wind Energy Association*, 2011.
[12] K. Graf, A. Hoeve, and S. Watin. Comparison of full 3D-RANS simulations with 2D-RANS/lifting line method calculations for the flow analysis of rigid wings for high performance multihulls. *Ocean Engineering*, 90:49–61, 2014.
[13] J. Hummel, D. Göhlich, and R. Schmehl. Automatic measurement and characterization of the dynamic properties of tethered membrane wings. *Wind Energy Science*, 4:41–55, 2019.
[14] M. Kheiri, F. Bourgault, V. Saberi Nasrabad, and S. Victor. On the aerodynamic performance of crosswind kite power systems. *Journal of Wind Engineering and Industrial Aerodynamics*, 181:1–13, 2018.
[15] R. B. Langtry and F. R. Menter. Correlation-based transition modeling for unstructured parallelized computational fluid dynamics codes. *AIAA Journal*, 47(12):2894–2906, 2009.
[16] R.C. Leuthold. Multiple-wake vortex lattice method for membrane wing kites. Master's thesis, Delft University of Technology, 2015.
[17] O. Lorillu, R. Weber, and J. Hureau. Numerical and experimental analysis of two-dimensional separated flows over a flexible sail. *J. Fluid Mech.*, 466(1):319–341, 2002.
[18] F. Menter and T. Esch. Elements of industrial heat transfer prediction. Proceedings of the 16th Brazilian Congress of Mechanical Engineering (COBEM), 2001.
[19] F. Menter, M. Kuntz, and R. Langtry. Ten years of industrial experience with the sst turbulence model. In K. Hanjalic, Y. Nagano, and M. Tummers, editors, *Turbulence, Heat and Mass Transfer 4*. Begell House, Inc., 2003.
[20] F.R. Menter. Two-equation eddy-viscosity turbulence models for engineering applications. *AIAA J.*, 32(8):1598–1605, 1994.
[21] J. Oehler and R. Schmehl. Aerodynamic characterization of a soft kite by in situ flow measurement. *Wind Energy Science*, 4(1):1–21, 2019.
[22] J. Oehler, M. van Reijen, and R. Schmehl. Experimental investigation of soft kite performance during turning maneuvers. *Journal of Physics: Conference Series*, 1037(052004), 2018.
[23] B. Python. Methodology improvement for performance assessment of pumping kite power wing. Master's thesis, Delft University of Technology and Ecole Polytechnique Fédérale de Lausanne, 2017.
[24] Mostafa A. Rushdi, Ahmad A. Rushdi, Tarek N. Dief, Amr M. Halawa, Shigeo Yoshida, and Roland Schmehl. Power prediction of airborne wind energy systems using multivariate machine learning. *Energies*, 13(9), 2020.
[25] S. Sachdeva. Impact of turning-induced shape deformations on aerodynamic performance of leading edge inflatable kites. Master's thesis, Delft University of Technology, 2017.
[26] R. Schmehl, editor. *Airborne wind energy: advances in technology development and research.* Springer, 2018.
[27] R. Smith and W. Shyy. Computation of aerodynamic coefficients for a flexible membrane airfoil in turbulent flow: A comparison with classical theory. *Physics of Fluids*, 8:3346–3353, 1996.
[28] J. Steiner. Towards the CSM-CFD modelling of membrane wings at high Reynolds numbers. Master's thesis, Delft University of Technology, 2018.
[29] K. Vimalakanthan, M. Caboni, J.G. Schepers, E. Pechenik, and P. Williams. Aerodynamic analysis of ampyx's airborne wind energy system. *Journal of Physics: Conference Series*, 1037(062008), 2018.
[30] I.M. Viola, P. Bot, and M. Riotte. Upwind sail aerodynamics: a RANS numerical investigation validated with wind tunnel pressure measurements. *International Journal of Heat and Fluid Flow*, 39:90–101, 2013.
[31] David C Wilcox. *Turbulence modeling for CFD.* DCW Industries, Inc., third edition, 2006.